# Supplementary Information for:

# Organic Emitters with Near-Unity Photoluminescence to Reinforce Buried Interface of Perovskite Solar Cells and Modules

Zhen-Yang Suo[a,†], Guo-Bin Xiao[a,†], Zhenhuang Su[b,†], Runmin Dong[a], Xijiao Mu[a], Xingyu Gao[b], Yiying Wu[c], Jing Cao[a,*]

[a]State Key Laboratory of Applied Organic Chemistry, Key Laboratory of Nonferrous Metal Chemistry and Resources Utilization of Gansu Province, College of Chemistry and Chemical Engineering, Lanzhou University, Lanzhou 730000, P.R. China
E-mail: caoj@lzu.edu.cn

[b]Shanghai Synchrotron Radiation Facility (SSRF), Shanghai Advanced Research Institute, Chinese Academy of Sciences, 239 Zhangheng Road, Shanghai 201204, China

[c]Department of Chemistry and Biochemistry, The Ohio State University, 100 West 18th Avenue, Columbus, Ohio 43210, United States

[†] Z. Y. Suo, G. B. Xiao and Z. H. Su contributed equally to this work.

E-mail: caoj@lzu.edu.cn (J. Cao)

## Contents

**1. Experimental section**

**2. Supporting figures**

**3. Supporting tables**

**4. Supporting references**

## 1. Experimental Section

### 1.1 Materials and chemicals

The following materials were used in the experiments: lead(II) iodide ($PbI_2$; 99.99%, TCI), methylammonium chloride (MACl), Methylammonium iodide (MAI), formamidinium iodide (FAI), Methylamine Hydrobromide (MABr), and Spiro-OMeTAD, $PbBr_2$, CsCl, CsI, were bought from Xi'an Polymer Light Technology in China, 4-methoxy-phenethylammonium iodide (MeO-PEAI, 99%, GreatCell Solar), tin(II) chloride dihydrate ($SnCl_2{\cdot}2H_2O$, 98%, Alfa), Urea (99.999%, aladdin), hydrochloric acid (HCl, 37 wt% in $H_2O$), thioglycolic acid ($C_2H_4O_2S$, 99%, Sigma-Aldrich), N,N-dimethylformamide (DMF, anhydrous, 99.8%, Sigma-Aldrich), dimethyl sulfoxide (DMSO, anhydrous, 99.9%, Sigma-Aldrich), 2-propanol (anhydrous, 99.5%, Sigma-Aldrich), chlorobenzene (anhydrous, 99.8%, Sigma-Aldrich), acetonitrile (ACN, anhydrous, 99.8%, Sigma-Aldrich), 4-tert-butylpyridine (t-BP, 98%, Sigma-Aldrich), bis(trifluoromethane)sulfonimide lithium salt(Li-TFSI, 99.95%, Sigma-Aldrich), FK209 Co(III) TFSI salt (Sigma-Aldrich) and Ethylacetate (EA, anhydrous, 99.8%, Sigma-Aldrich).

The single crystal of $MAPbBr_3$ was synthesized using the procedure reported in the literature[1]. The $MAPbBr_3$ single crystals were synthesized using 1.4 M of MABr (99.99%) and $PbBr_2$ in dimethylformamide (DMF, 98% anhydrous, Sigma Aldrich). After filtering using 0.45 μm PTFE filter, the solution was heated at 90 ℃ for 2 h. The single crystals were collected and washed with acetonitrile and dimethyl-ether 3 times, which was dried at 100 ℃ for 30 min.

The two organic luminescent molecules were prepared using the synthesis methods reported in the literature[2, 3].

### 1.2 Small-sized Solar Cell Fabrication

The device with an architecture of FTO glass/$SnO_2$/$Cs_{0.08}FA_{0.92}PbI_3$ /Spiro-OMeTAD/Au structure was fabricated. FTO glass (AGC-A22-85) substrates were sequentially sonicated in acetone, detergent, and Isopropyl Alcohol for 15 min each. And then the $SnO_2$ electron transport layer was prepared utilizing a chemical bath deposition method. The specific experimental procedure is as follows: Briefly, 1.25 g of urea and 275 mg of $SnCl_2{\cdot}2H_2O$ were dissolved in 100 mL of deionized water. Then, 1.25 mL of HCl and 25 μL of TGA were added into this solution. The cleaned FTO substrates were horizontally placed into the vessel and the reaction was kept at 90 ℃ for 6 h. After the reaction is completed, the FTO/$SnO_2$ substrate was removed

from the reaction box and cleaned via sonication with deionized water and IPA for 2 min each. The substrate was then annealed in an ambient environment at 190 °C for 60 min, after cooling down to room temperature. After UV-ozone treatment of the substrates for 15 min, we used 4′-(4-(diphenylamino)phenyl)-5′-phenyl[1,1′:2′,1″-terphenyl]-4-carbonitrile (TPA) and 4′-(4-(9H-carbazol-9-yl)phenyl)-5′-phenyl-[1,1′:2′,1″-terphenyl]-4-carbonitrile (Cz) to treat the interface of $SnO_2$ layer by spin-coating the solutions in dichloromethane with the concentrations of 0.1 mg/mL, 0.3 mg/mL, and 0.5 mg/mL on the $SnO_2$ substrates at 3000 rpm for 30 s.

The perovskite precursor solution (1.5 M) was prepared by adding 726.1 mg of $PbI_2$ (excess 5 mol%), 237.32 mg of formamidium iodide (FAI), 31.18 mg of CsI and 2.84 mg of $MAPbBr_3$ (0.5 mol%) into 200 μL of Dimethyl sulfoxide (DMSO) and 800 μL of N,N-Dimethylformamide (DMF) mixture. After the interface treat, 60 μL of perovskite precursor solution was spin-coated on top of the $SnO_2$ substrate through a two-step process. The first step was 1000 rpm for 10 s with an acceleration of 200 rpm/s. The second step was 5000 rpm for 30 s with an acceleration of 2000 rpm/s, 200 μL of EA was dripped onto the substrate during spinning. Afterwards, the substrate was put onto the hotplate and heated at 120 °C for 40 min. After the perovskite film was cooled down to room temperature, 80 μL of MeO-PEAI solution (5 mg/mL in isopropanol) was spin-coated on the perovskite film at 3000 rpm for 30 s. For Spiro-OMeTAD solution of 73 mg/mL in chlorobenzene, 18 μL Li-TFSI solution (520 mg/mL in acetonitrile), 29 μL of Co-TFSI solution (300 mg/mL in acetonitrile) and 30 μL of 4-tertbutylpyridine was sequentially added and spin-coated on the FTO/$SnO_2$/perovskite substrate at 3000 rpm for 30 s. Finally, a gold layer approximately 80 nm thick was evaporated on the Spiro-OMeTAD layer as the electrode, and the aperture area of the certified device is 0.0999 $cm^2$.

All the processes mentioned in this work were conducted in a controlled air environment with regulated humidity and temperature, including the entire process of laser preparation of the perovskite module, with the temperature maintained at 20-25°C and the humidity controlled to be less than 20% RH.

**1.3 Peeling-off buried interface process**

For the removal of the buried interface, a smooth surface FTO substrate (Asahi Glass) was employed as the base to reveal the underlying perovskite film. UV glue (LOCTITE AA3528) was applied onto a clean glass slide and carefully layered on the perovskite films. The pressure was applied to eliminate any remaining air bubbles.

Subsequently, the adhesive was solidified under a 365 nm ultraviolet light for approximately 1 minute. Finally, opposing forces were exerted on the glass slide and the bonded perovskite films were peeled off from the $SnO_2$-based substrate, to fully expose the buried interface of the perovskite film.

**1.4 Module Fabrication**

Perovskite solar modules, with 5 sub-cells connected in series, were fabricated the device on FTO glass substrates with a size of 5 × 5 $cm^2$. The module's series interconnection was established through the patterning of P1, P2, and P3 lines using a laser scribing system with a wavelength of 1064 nm and a power output of 20 W (Suzhou Microtreat Intelligent Technology Co.,Ltd). The FTO substrate was pre-patterned for P1 (a width of 20 μm) by means of 36% laser power under a speed of 500 mm/s with a frequency of 400 kHz and pulse width of 30 ns. The subsequent processes for the preparation of $SnO_2$ substrates are the same than the small area device procedures. Moreover, the deposition procedure for the perovskite precursor closely resembled that of the small-scale solar cells, with the notable distinction being the variation in concentration of the perovskite precursor. In brief, 1.4 M of perovskite precursor was employed to do the perovskite layer by using spin-coated method, the addition of the antisolvent took the same duration as that for the small-scale cells. The point of distinction lies in the utilization of 400 μL of antisolvent. After spin-coating, the brown and transparent perovskite film is placed onto the hot plate. The perovskite films were annealed at 120 ºC for 40 min. Upon cooling to room temperature, the procedures for depositing the MeO-PEAI passivation layer and the Spiro-OMeTAD layer adhere to a methodology similar to that utilized for smaller-scale devices. The P2 lines (with a width of 200 μm) underwent etching prior to the Au evaporation process step, employing an average laser power of 27%, a speed of 500 mm/s, a frequency of 100 kHz, and a pulse duration of 30 ns. The distance between P1 and P2 is approximately 50 μm. When a gold layer 100 nm thick was deposited, the P3 line (a width of 30 μm) was fabricated under the same scribing conditions as the P2 line. The distance between P1 and P3 was around 330 μm and the geometric fill factor (GFF) was around 95.44%. Additionally, laser edge cleaning was applied to the perovskite components, resulting in a light-receiving area of 11.455 $cm^2$ for the perovskite component.

**1.5 Device Characterization**

The current density-voltage (J-V) characteristics of the devices were measured

using a Keithley 2601B Source Meter under standard AM1.5 G illumination (Newport, calibrated by a certified silicon cell), The J-V curves were measured by forward scan (-0.1 to 1.22 V) and reverse scan (1.22 to -0.1 V) at a scanning rate of 100 mV/s. While the modules were measured using a reverse scan (from 6.1 V to -0.1 V) and a forward scan (from -0.1 V to 6.1 V) under a constant scan speed of 100 mV/s. Incident photon-to-electron conversion efficiency (IPCE) were measured on a computer-controlled IPCE system containing a Xenon lamp, a monochromator and a Keithley multimeter. The apparatus was calibrated with the certified silicon solar cell and the IPCE data were collected at DC mode. The X-ray diffraction (XRD) data were collected using CuKa radiation on a Rigaku RINT-2500 X-ray diffractometer. The surface images were recorded on a SEM-4800 field-emission scanning electron microscope (SEM). UV-vis absorption spectra were obtained from a cary-5000 UV-vis spectrophotometer. The Time-resolved photoluminescence (PL) spectra were measured by Edinburgh Instruments FLS920 spectrometer. The cyclic voltammetry (CV) were tested by an electrochemical workstation (CHI660E). The FT-IR spectra were recorded on Nicolet Nexus-670 with KBr pellets. The samples prepared in the same way as the perovskite film in PSCs. The synchrotron-based in situ grazing-incidence wide-angle X-ray scattering (GIWAXS) was conducted by the BL14B1 beamline at Shanghai Synchrotron Radiation Facility (SSRF). The X-ray beam used had a wavelength of 1.2398 Å at a grazing incidence angle of 0.5° and an energy of 10 KeV. Two-dimensional (2D) Grazing Incidence Wide-Angle X-ray Scattering (GIWAXS) patterns were obtained using a MarCCD 225 detector, with a distance of 330 mm between the samples and the detector. Analysis of the 2D GIWAXS patterns was performed using the FIT2D software. The GIWAXS patterns were presented in scattering vector (q) coordinates, calculated with the formula $q = 4\pi\sin\theta/\lambda$, where $\theta$ is half of the diffraction angle and $\lambda$ is the incident wavelength. During the processing of the GIWAXS data, the q vector was calibrated by measuring X-ray Diffraction (XRD) from a Lanthanum hexaboride reference sample.

**1.6 X-ray photoelectron spectroscopy (XPS) testing and analysis**

To investigate the interaction between perovskite and two types of luminescent materials clearly, the perovskite precursor solution was mixed with luminescent molecules. After that, the material was washed and dried using diethyl ether antisolvent, followed by X-ray photoelectron spectroscopy (XPS) analysis.

**1.7 Long-term device stability characterization**

The stabilities were tested by fabricating the PSCs with the FTO/$SnO_2$/perovskite/Phthalocyanine (Pc)/Au configuration. The encapsulated devices were maintained at the maximum power point (MPP) using a MPP tracking algorithm under 1 Sun illumination according to ISOS-L-1 protocol.

**1.8 Computational Details**

In this study, our computational methodology was structured to meticulously investigate the structural and electronic properties of molecular modifiers on electronic transport material surfaces. The approach consisted of two primary stages: computational modeling using Density Functional Theory (DFT)[4] and subsequent detailed analyses employing the Multiwfn-3.5. The foundational aspect of our study involved the application of DFT, a quantum mechanical modeling method used to investigate the electronic structure of many-body systems. This modeling was performed using the Quickstep module[5] in CP2K-2022 version[6]. In our computational study, we utilized the Goedecker-Teter-Hutter (GTH) pseudopotentials[7] and the Triple-Zeta Valence with Polarization (TZVP) basis set in gaussian and augmented plane waves (GAPW)[8] to accurately represent the electronic states of the molecules. The cutoff energy was set at 1000 eV, ensuring a comprehensive representation of the wavefunctions. For the convergence criteria, we maintained a strict self-consistent field (SCF) threshold of $1e^{-8}$ Hartree and a geometric optimization convergence limit of $-2e^{-2}$, ensuring precise and reliable calculations of electronic structures and molecular geometries. These parameters collectively provided a balance between computational efficiency and the accuracy required for our molecular simulations. Within this framework, the focus was on calculating electronic structures, molecular geometries, and electronic transport behaviors. DFT serves as a reliable predictor of these properties, essential for the initial understanding of how molecular modifiers interact with material surfaces. Upon obtaining the basic electronic structure information from DFT calculations, we employed the Multiwfn-3.5[9] for a series of advanced analyses, each contributing unique insights into the molecular and electronic characteristics of the system: Using Multiwfn, we calculated the restrained electrostatic potential (RESP) charges[10]. This approach is crucial for accurately determining the charge distribution within the molecules, particularly in relation to electrostatic interactions both within the molecules and between the molecules and the material surfaces. The projected local density of states (PLDOS) analysis provides a nuanced understanding of the electronic states associated with specific atoms or

groups within the molecules. The PLDOS reveals how the electronic states at the atomic or molecular level contribute to the overall electronic transport properties. Through differential charge density analysis, we identified the changes in electron density because of molecular interactions. This analysis highlights electron-rich and electron-deficient regions, offering insights into the electronic rearrangements upon surface modification. Our methodical approach, combining DFT calculations with advanced analytical techniques in Multiwfn, provided a comprehensive understanding of the molecular and electronic dynamics at play. This dual-stage methodology allowed us to delve deeply into how molecular modifiers influence the electronic transport properties of material surfaces, guiding future innovations in material design.

**1.9 Defects in perovskite**

We also investigated the effect of Cz and TPA on the trap density of perovskite films for the electron-only devices with FTO/$SnO_2$/perovskite/PCBM/Au structure by space-charge limited current (SCLC) measurements. The trap density ($N_t$) of perovskite films can be calculated by the following equation:

$$N_t = \frac{2\varepsilon_0 \varepsilon V_{TFL}}{eL^2}$$

where $\varepsilon_0$ ($8.854 \times 10^{-12}$ F/m), $\varepsilon$ (46.9 to reference) $V_{TFL}$, e, and L (600 nm) are permittivity of vacuum, relative dielectric constant, trap-filled limit voltage, elementary charge, and the thickness of perovskite films, respectively.

**1.10 Urbach energies (Eu)**

Urbach energies (Eu) were also compared because the low defect concentration of the perovskite thin film responsible for the high performance was because of the superiority of the structural quality during the crystal formation of perovskites. Eu for the perovskite films was calculated from the ultraviolet (UV)–visible absorption spectra using the following equation: $\alpha = \alpha_0 \exp(h\nu/Eu)$, in which $\alpha$ is the absorption coefficient and $h\nu$ is the photon energy.

## 2. Supporting figures

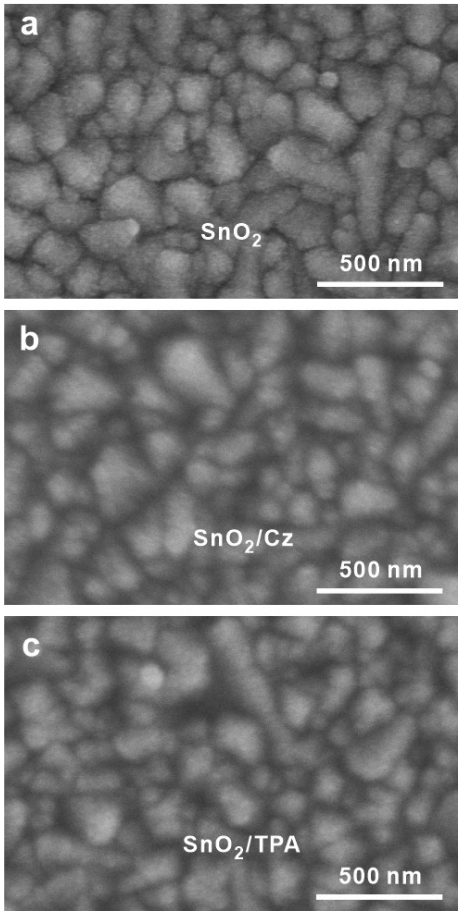


Fig. S1. SEM images of $SnO_2$ films without (a), with Cz (b) and TPA treatment (c).

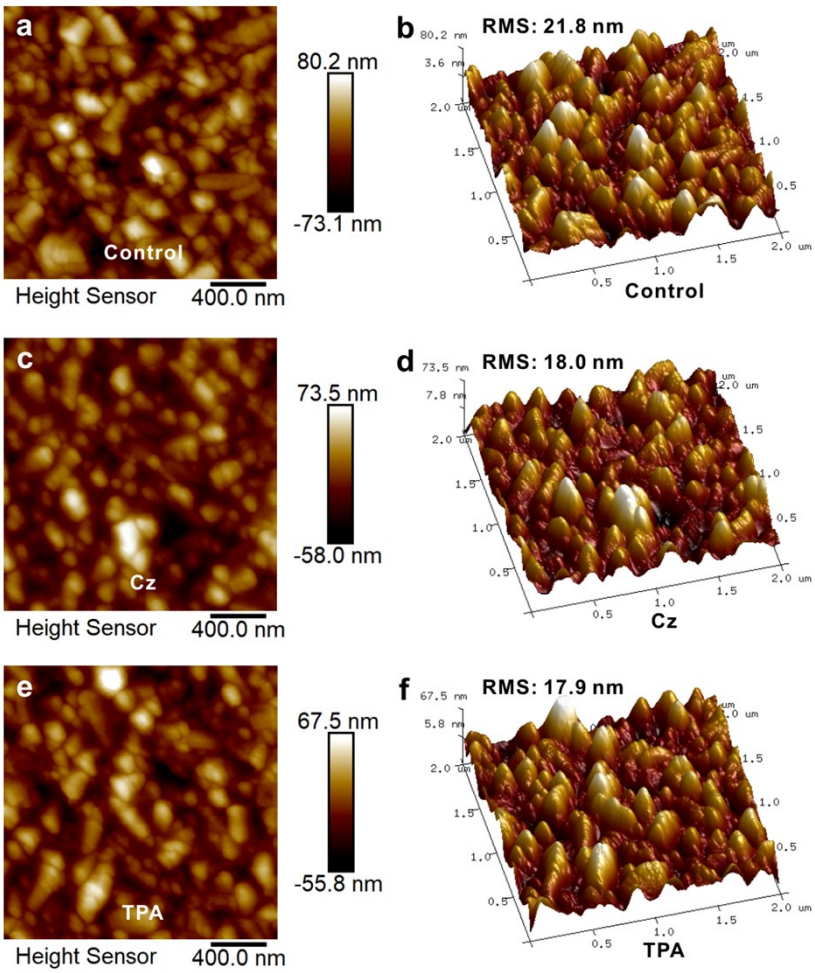


Fig. S2. AFM images of $SnO_2$ films without (a, b), with Cz (c, d) and with TPA (e, f) treatment.

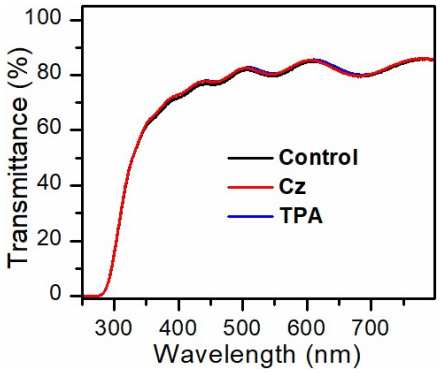


Fig. S3. Transmission spectra of $SnO_2$ films without and with Cz and TPA treatment.

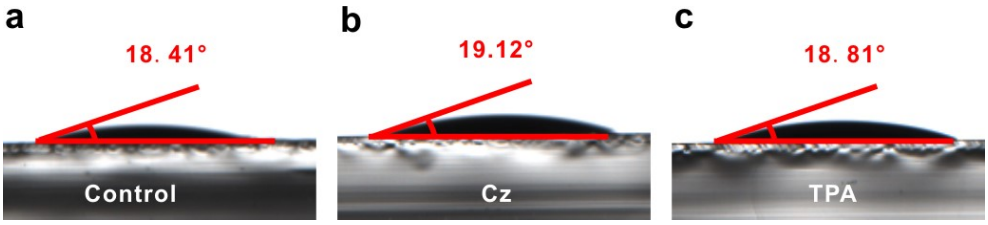


Fig. S4. Contact angle tests of the perovskite precursor solution on $SnO_2$ films without (a), with Cz (b) and with TPA (c).

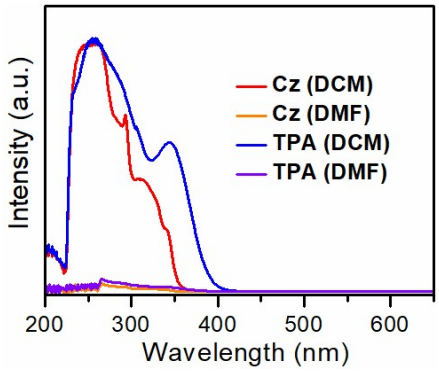


Fig. S5. UV-vis spectra of Cz and TPA dissolved into $CH_2Cl_2$ and DMF solution.

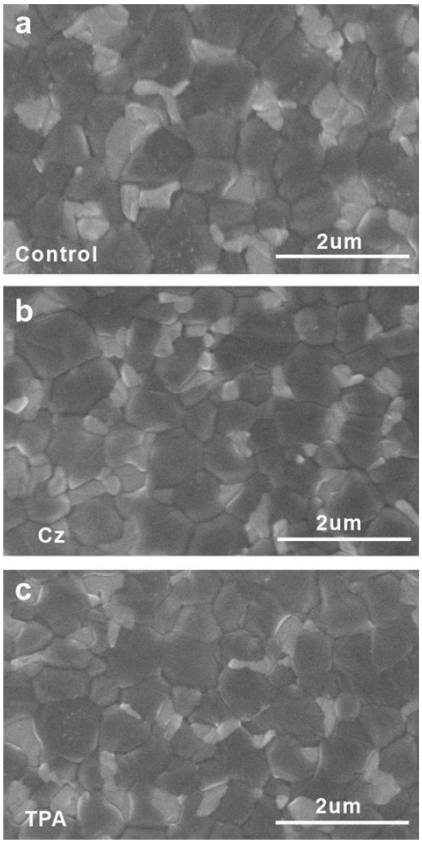


Fig. S6. SEM images of perovskite films deposited on $SnO_2$ substrates without (a), with Cz (b) and TPA treatment (c).

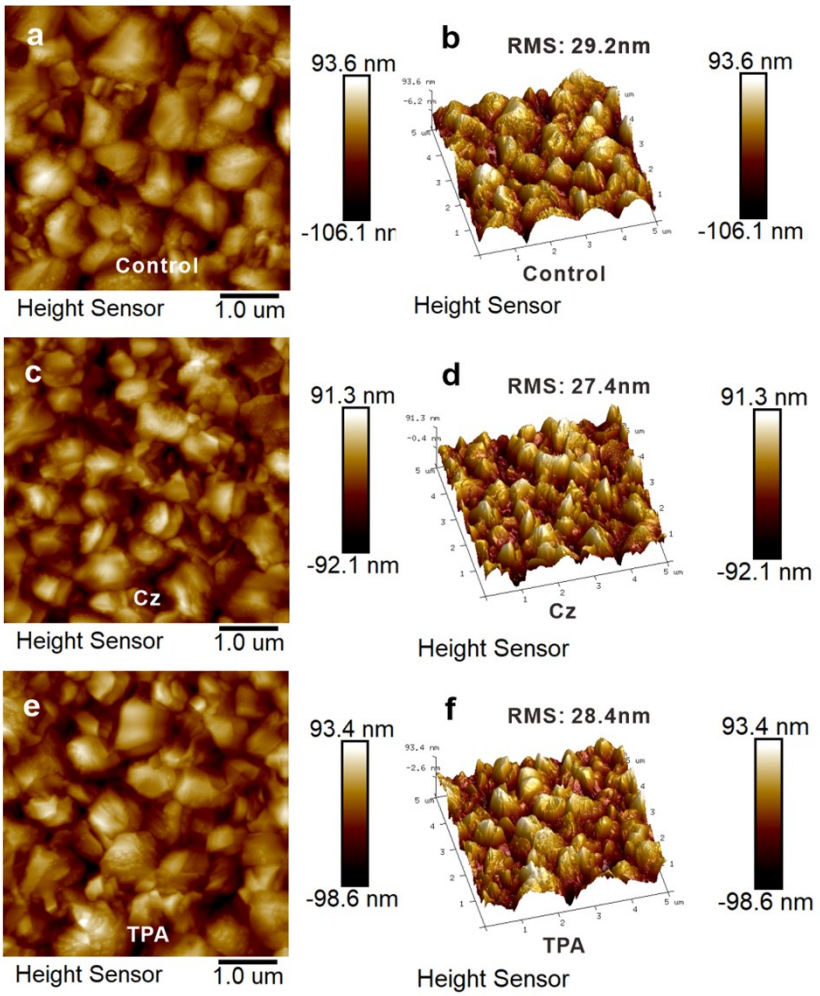


Fig. S7. AFM images of perovskite films on deposited on $SnO_2$ substrates without (a, b), with Cz (c, d) and TPA treatment (e, f).

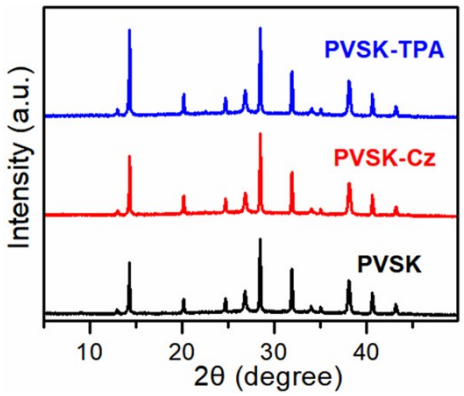


Fig. S8. X-ray diffraction (XRD) patterns of perovskite films prepared on different substrates.

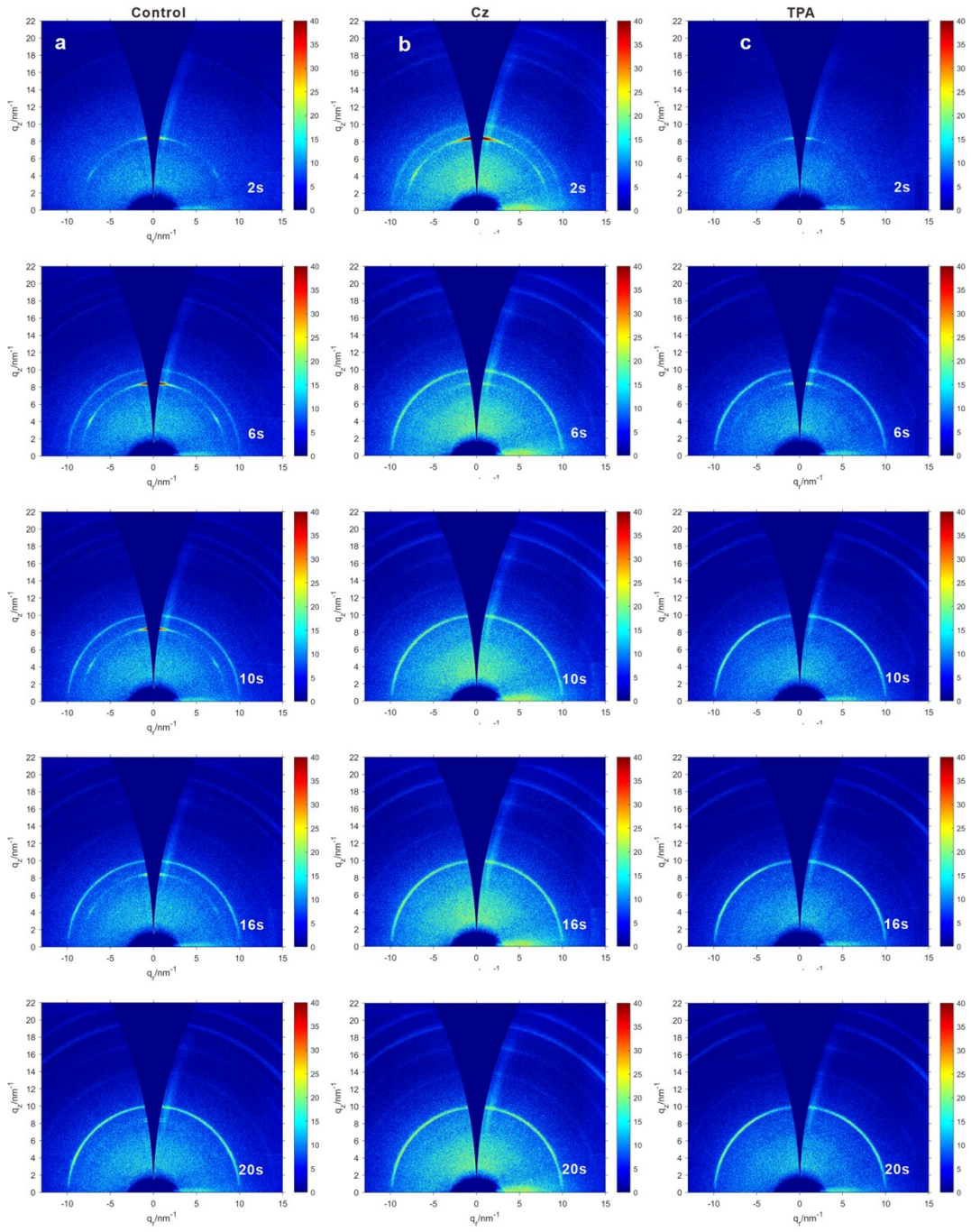


Fig. S9. In-situ perovskite spin-coating experiments conducted on $SnO_2$ substrates without (a), with Cz (b) and TPA treatment (c). The data indicates that the perovskite films spin-coated on treated substrates can undergo a faster transition to light-absorbing perovskite phase compared to the film on untreated $SnO_2$ substrate.

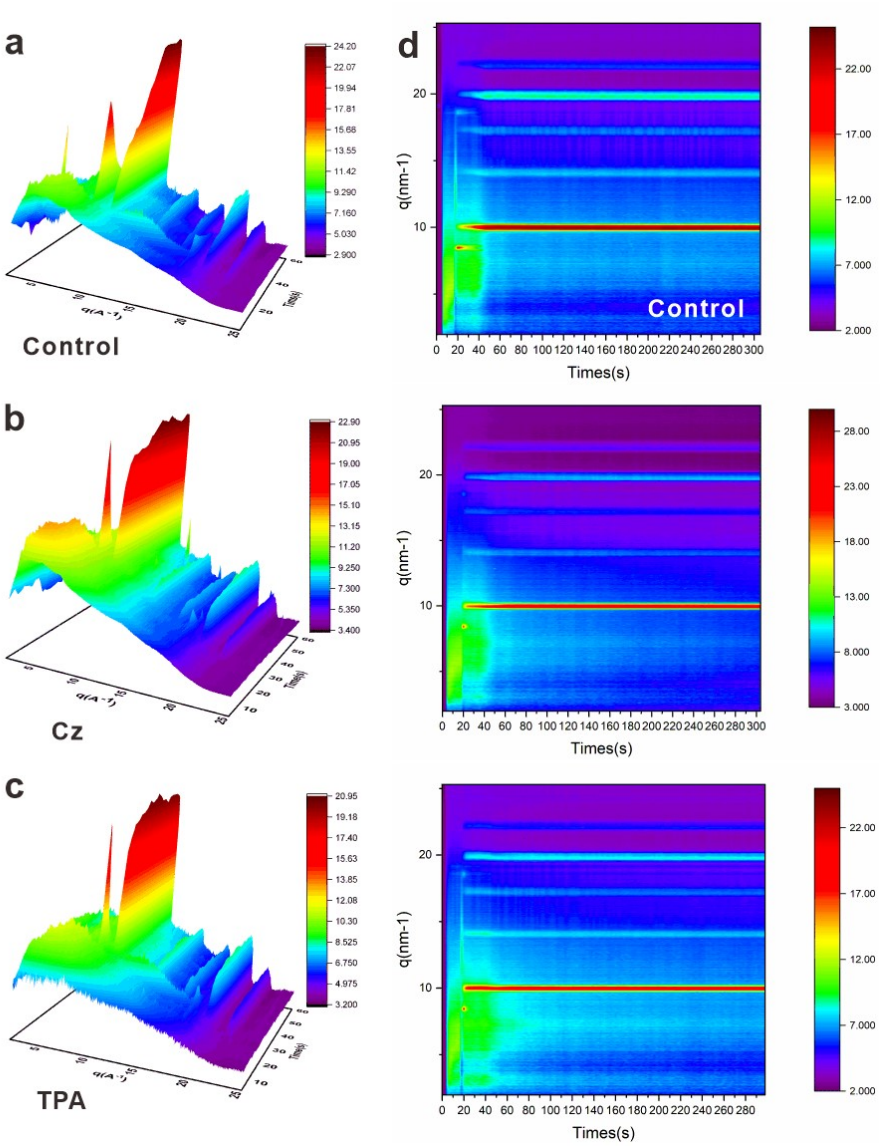


Fig. S10. In-situ perovskite spin-coating experiments conducted on $SnO_2$ films without (a, d), with Cz (b, e) and TPA (c, f) treatment. In the perovskite spin-coating experiments, in-situ GIWAXS data were collected. Upon the addition of the anti-solvent, the perovskite film prepared on the untreated $SnO_2$ substrate exhibited an intermediate phase before eventually transforming into the light-absorbing perovskite phase after a period and heating. In contrast, when spin-coating perovskite on the $SnO_2$ substrate modified with emitters, a similar intermediate phase appeared upon the addition of the anti-solvent, but its duration was shorter, and the rapid transformation into the light-absorbing perovskite phase occurred swiftly. Heating also facilitated a faster growth of the perovskite film.

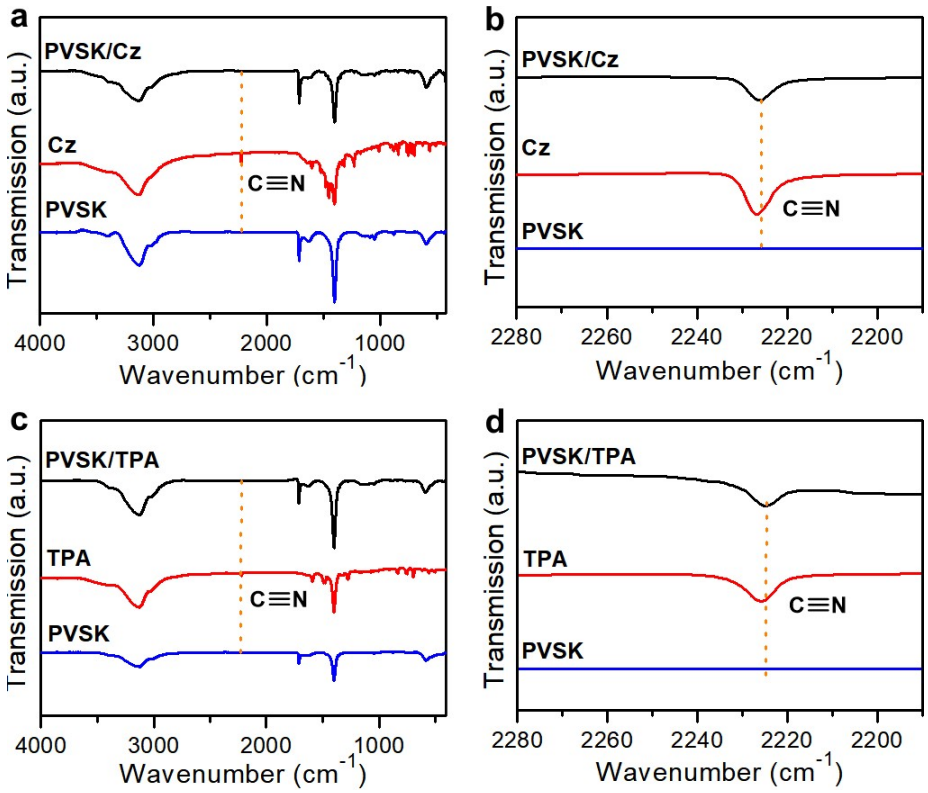


Fig. S11. FT-IR spectra of perovskite (PVSK), Cz-modiifed perovskite (a, b) and TPA-modiifed perovskite (c, d) samples.

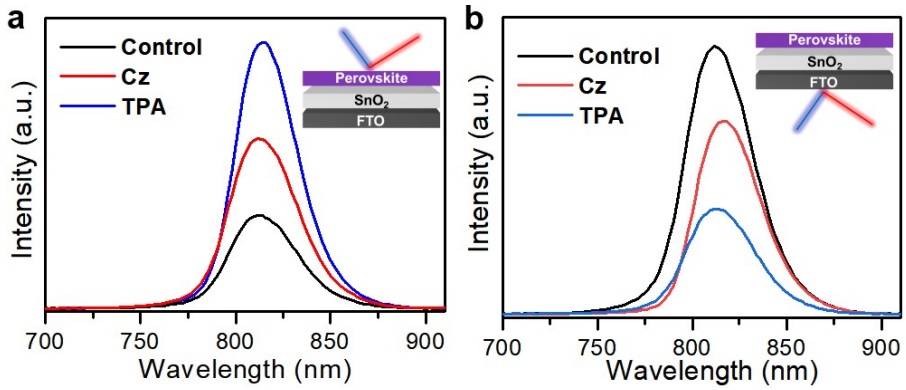


Fig. S12. Steady-state PL spectra of two substrate-treated and untreated perovskite films excited from the perovskite film side (a) and bottom (b). TPA-based film had the largest fluorescence intensity excited from substrate bottom than the control and Cz-based sample, while it had the smallest fluorescence intensity excited from from perovskite film side. These verify the emitters (especially for TPA) could stabilize the buried interface by modulating the interfacial perovskite film crystallization.

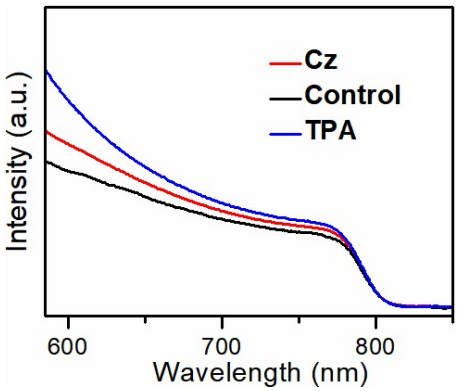


Fig. S13. UV-vis absorption spectra of perovskite films without and with modification.

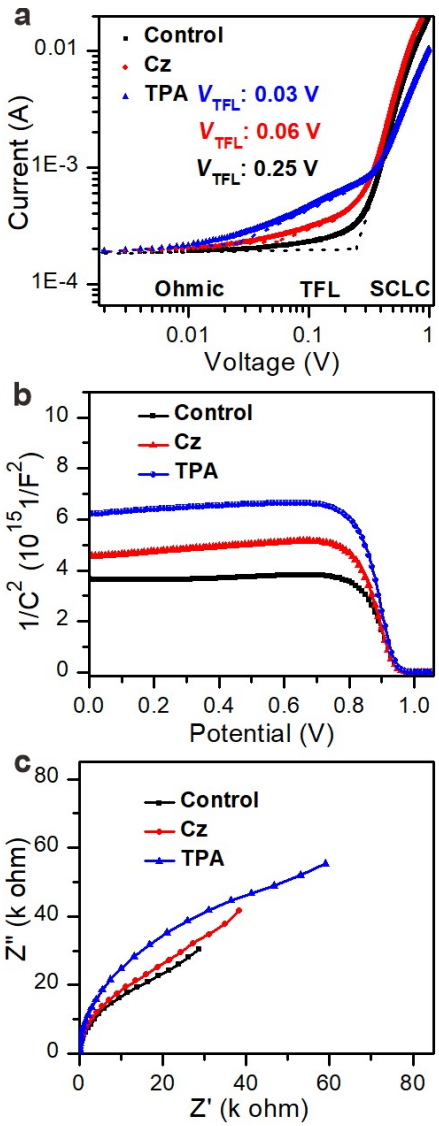


Fig. S14. Space-charge-limited current (a), Mott-Schottky (b) and Impedance(c) analyses of the target and control devices.

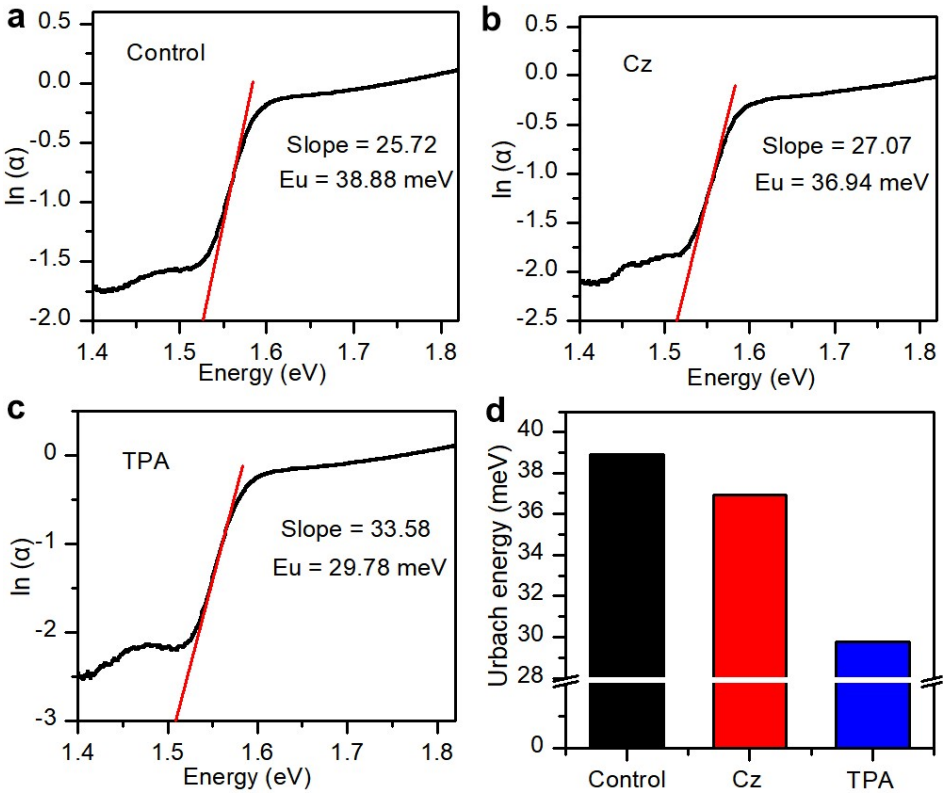


Fig. S15. Urbach energy values for perovskite films prepared on various substrates. Comparative analysis indicates that the Urbach energy of perovskite films modified with Cz and TPA molecules is smaller than that of the control sample. This suggests the modification of Cz and TPA improve the quality of perovskite with fewer defects.

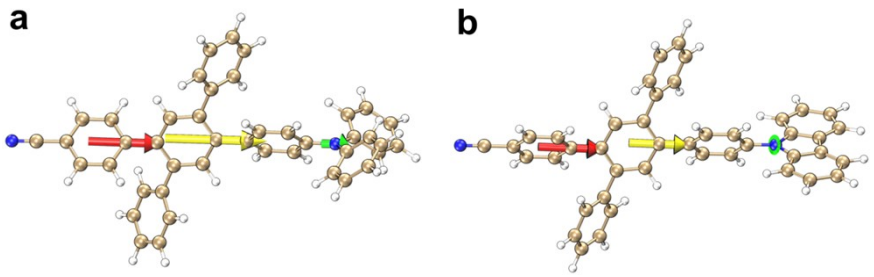


Fig. S16. Dipole moment decomposition analysis by molecular fragments of the TPA (a) and Cz (b).

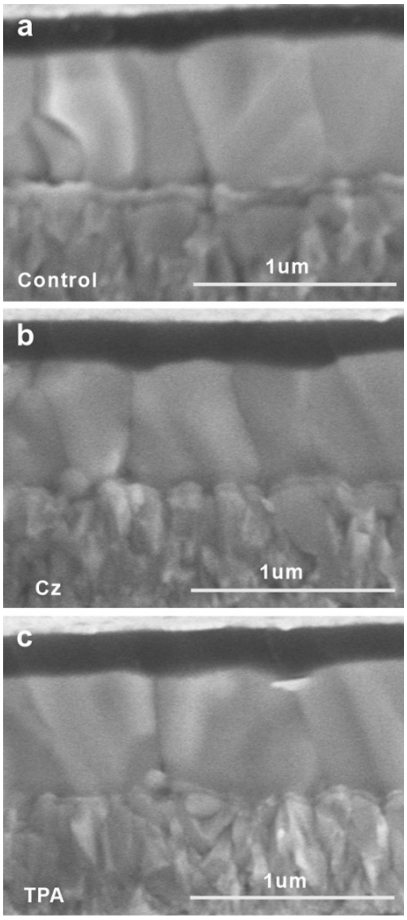


Fig. S17. Cross-sectional SEM images of perovskite films deposited on $SnO_2$ films without (a), with Cz (b) and TPA (c) treatment.

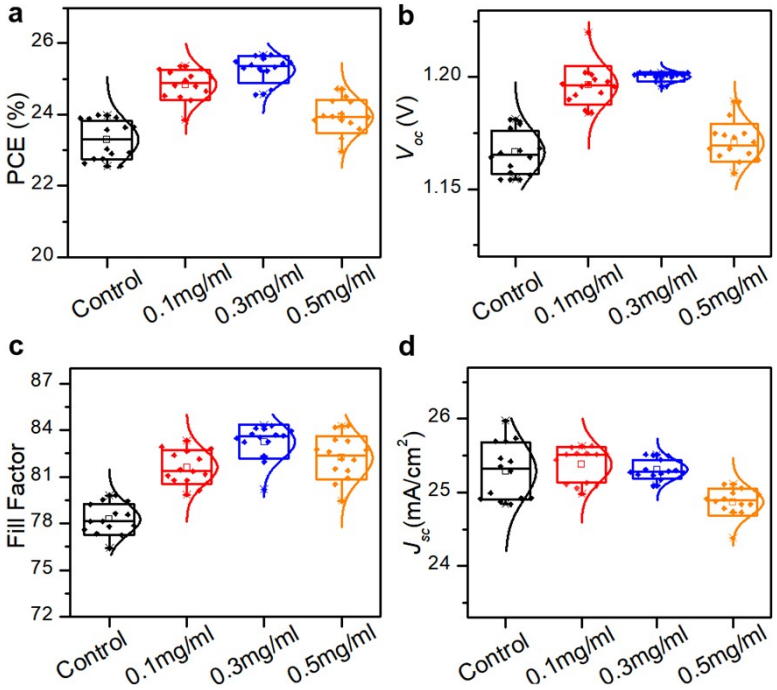


Fig. S18. Histograms of cell efficiencies among 15 cells of PSCs without and with modification.

230017163974

中国认可
国际互认
检测
TESTING
CNAS L8490

Test and Calibration Center of New Energy Device and Module,
Shanghai Institute of Microsystem and Information Technology,
Chinese Academy of Sciences (SIMIT)

# Measurement Report

**Report No. 23TR110302**

| | |
|---|---|
| **Client Name** | Lanzhou University |
| **Client Address** | 222 South Tianshui Road, Lanzhou 73000,Gansu Province |
| **Sample** | Perovskite solar cell |
| **Manufacturer** | Lanzhou University |
| **Measurement Date** | 3rd November, 2023 |

| | | |
|---|---|---|
| **Performed by:** | Qiang Shi Qiang Shi | **Date:** 03/11/2023 |
| **Reviewed by:** | Wenjie Zhao Wenjie Zhao | **Date:** 03/11/2023 |
| **Approved by:** | Yucheng Liu Yucheng Liu | **Date:** 03/11/2023 |

**Address:** No.235 Chengbei Road, Jiading, Shanghai **Post Code:**201800

**E-mail:** solarcell@mail.sim.ac.cn **Tel:** +86-021-69976921

| Sample Information | |
|---|---|
| Sample Type | Perovskite solar cell |
| Serial No. | LZU7-2# |
| Lab Internal No. | 23110301-2# |
| Measurement Item | I-V characteristic |
| Measurement Environment | 25.1±2.0°C,47.3±5.0%R.H |

| Measurement of I-V characteristic | |
|---|---|
| **Reference cell** | PVM 1121 |
| **Reference cell Type** | mono-Si, WPVS, calibrated by NREL (Certificate No. ISO 2075) |
| **Calibration Value/Date of Calibration for Reference cell** | 144.53mA/ Feb. 2023 |
| **Measurement Conditions** | Standard Test Condition (STC):<br>Spectral Distribution: AM1.5 according to IEC 60904-3 Ed.3,<br>Irradiance: 1000±50W/m$^2$, Temperature: 25±2°C |
| **Measurement Equipment/ Date of Calibration** | AAA Steady State Solar Simulator (YSS-T155-2M) / July.2023<br>IV test system (ADCMT 6246) / June. 2023<br>Measuring Microscope (MF-B2017C) / July.2023<br>SR Measurement system (CEP-25ML-CAS) / April.2023 |
| **Measurement Method** | I-V Measurement:<br>Logarithmic sweep in both directions (Voc to Isc and Isc to Voc) during one flash based on IEC 60904-1:2020.<br>Spectral Mismatch factor was calculated according to IEC 60904-7 and I-V correction according to IEC 60891. |
| **Measurement Uncertainty** | Area: 1.0%(k=2); Isc: 1.9%(k=2); Voc: 1.0%(k=2);<br>Pmax: 2.3%(k=2); Eff: 2.5%(k=2) |

**====Measurement Results ====**

| | Forward Scan (Isc to Voc) | Reverse Scan (Voc to Isc) |
|---|---|---|
| Area | 9.99 $mm^2$ | |
| Isc | 2.497 mA | 2.505 mA |
| Voc | 1.192 V | 1.192 V |
| Pmax | 2.472 mW | 2.507 mW |
| Ipm | 2.358 mA | 2.395 mA |
| Vpm | 1.048 V | 1.047 V |
| FF | 83.04 % | 83.92 % |
| Eff | 24.74 % | 25.09 % |

- Spectral Mismatch Factor: SMM=0.9920.
- Designated illumination area defined by a thin mask was measured by measuring microscope.
- Test results listed in this measurement report refer exclusively to the mentioned measured sample.
- The results apply only at the time of the test, and do not imply future performance.

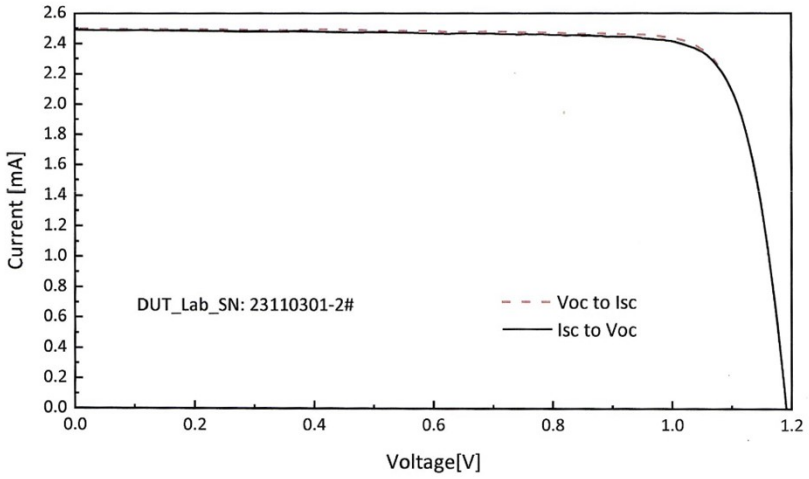


**Fig.1** I-V curves of the measured sample



Fig. S19. Certified performance of small-area PSCs based on substrates treated with TPA. The certified efficiency is 25.09 % under reverse scan (short-circuit current (*Isc*) of 2.505 mA, $V_{OC}$ of 1.192 V, FF of 83.92% and area of 9.99 $mm^2$). Furthermore, the certified efficiency exhibits a negligible hysteresis.

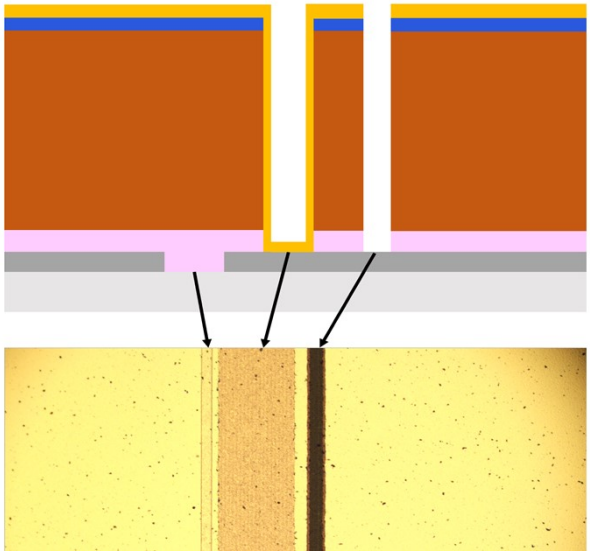

Fig. S20. The geometric design drawings and microscopically recorded photographs of the perovskite component, along with a rough calculation, indicate a geometric filling factor of (GFF) approximately 95.44% for the perovskite component.

Test and Calibration Center of New Energy Device and Module,
Shanghai Institute of Microsystem and Information Technology,
Chinese Academy of Sciences (SIMIT)

# Measurement Report

**Report No. 23TR121501**

| | |
|---|---|
| **Client Name** | Lanzhou University |
| **Client Address** | 222 South Tianshui Road, Lanzhou 73000,Gansu Province |
| **Sample** | Perovskite PV mini-module |
| **Manufacturer** | Lanzhou University |
| **Measurement Date** | 15th December, 2023 |

| | | |
|---|---|---|
| **Performed by:** | Qiang Shi | **Date:** 15/12/2023 |
| **Reviewed by:** | Wenjie Zhao | **Date:** 15/12/2023 |
| **Approved by:** | Yucheng Liu | **Date:** 15/12/2023 |

**Address:** No.235 Chengbei Road, Jiading, Shanghai **Post Code:**201800
**E-mail:** solarcell@mail.sim.ac.cn **Tel:** +86-021-69976921

**Sample Information**

| | |
|---|---|
| Sample Type | Perovskite PV mini-module |
| Serial No. | LZU-1 |
| Lab Internal No. | 23121501-1# |
| Measurement Item | I-V characteristic |
| Measurement Environment | 24.3±2.0°C, 44.2±5.0%R.H |

**Measurement of I-V characteristic**

| | |
|---|---|
| **Reference cell** | PVM1121 |
| **Reference cell Type** | mono-Si, WPVS, calibrated by NREL (Certificate No. ISO 2075) |
| **Calibration Value/Date of Calibration for Reference cell** | 144.53mA/ Feb. 2023 |
| **Measurement Conditions** | Standard Test Condition (STC):<br>Spectral Distribution: AM1.5 according to IEC 60904-3 Ed.3,<br>Irradiance: 1000±50W/m$^2$, Temperature: 25±2°C |
| **Measurement Equipment/ Date of Calibration** | AAA Steady State Solar Simulator (YSS-T155-2M) / July.2023<br>IV test system (ADCMT 6246) / June. 2023<br>Measuring Microscope (MF-B2017C) / July.2023<br>SR Measurement system (CEP-25ML-CAS) / April.2023 |
| **Measurement Method** | I-V Measurement:<br>Logarithmic sweep in both directions (Voc to Isc and Isc to Voc) during one flash based on IEC 60904-1:2020;<br>Spectral Mismatch factor was calculated according to IEC 60904-7 and I-V correction according to IEC 60891. |
| **Measurement Uncertainty** | Area: 1.1%(k=2); Isc: 2.1%(k=2); Voc: 1.0%(k=2);<br>Pmax: 2.4%(k=2); Eff: 2.5%(k=2) |

Report No. 23TR121501

====Measurement Results ====

| | Forward Scan (Isc to Voc) | | Reverse Scan (Voc to Isc) | |
|---|---|---|---|---|
| Area(AP) | 11.438 $cm^2$ | | | |
| Active Area(AA) | 10.958 $cm^2$ | | | |
| Isc | 52.961 | mA | 52.895 | mA |
| Voc | 6.029 | V | 6.018 | V |
| Pmax | 256.564 | mW | 261.097 | mW |
| Ipm | 50.110 | mA | 50.600 | mA |
| Vpm | 5.120 | V | 5.160 | V |
| FF | 80.35 | % | 82.02 | % |
| Eff(AP) | 22.43 | % | 22.83 | % |
| Eff(AA) | 23.41 | % | 23.83 | % |

- Spectral Mismatch Factor SMM=0.9910.
- Aperture area(AP) and active area(AA) were measured by the measuring microscope.
- Aperture area was the active area plus interconnection areas between sub cells.
- No mask was used. The influence of reflections outside the assigned area was not considered.
- Test results listed in this measurement report refer exclusively to the mentioned test sample.
- The results apply only at the time of the test, and do not imply future performance.

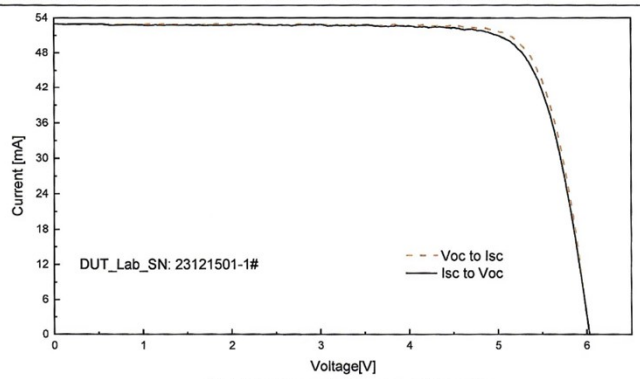


**Fig.1** I-V curves of the measured sample

**-------End of Report-------**

**3 / 3**

Fig. S21. Certified performance of large-area perovskite solar mini-module based on substrates treated with TPA. The certified efficiency is 22.83 % (Aperture area) and 23.83% (Active area), under reverse scan (short-circuit current (*Isc*) of 52.895 mA, $V_{OC}$ of 6.018 V, FF of 82.02% and aperture area of 11.438 $cm^2$, active area of 10.958 $cm^2$). The module comprises five individual cells. Furthermore, this represents one of the higher efficiencies reported for perovskite modules in the current literature.

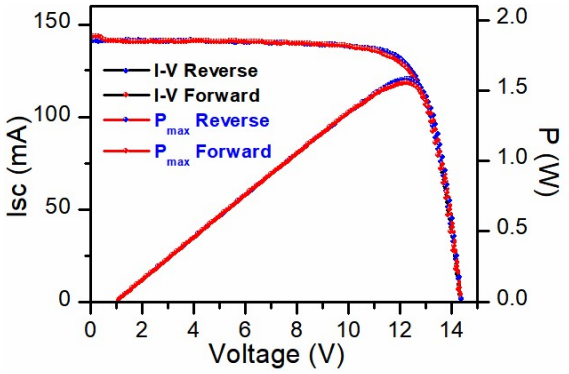


Fig. S22. I-V efficiency of the large-area module (72 $cm^2$).

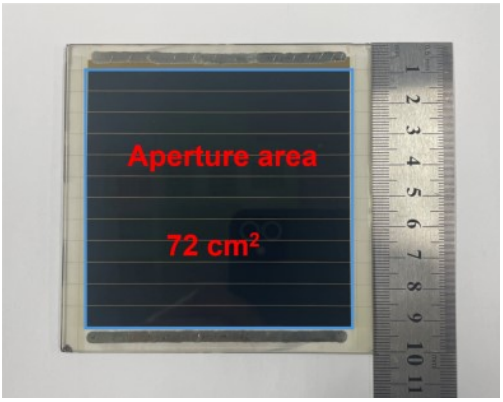


Fig. S23. Large-area module images. By employing a process similar to that of small-area modules and through careful design, we have successfully fabricated large-area modules with an efficiency of 21.91%. The only difference from the small-area modules lies in the width of the sub-cells.

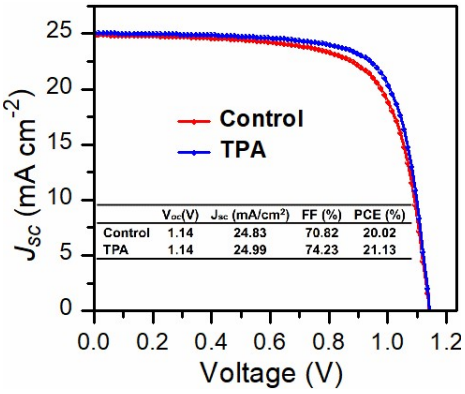


Fig. S24. Best *J-V* data of PSCs with phthalocyanine as hole transport materials.

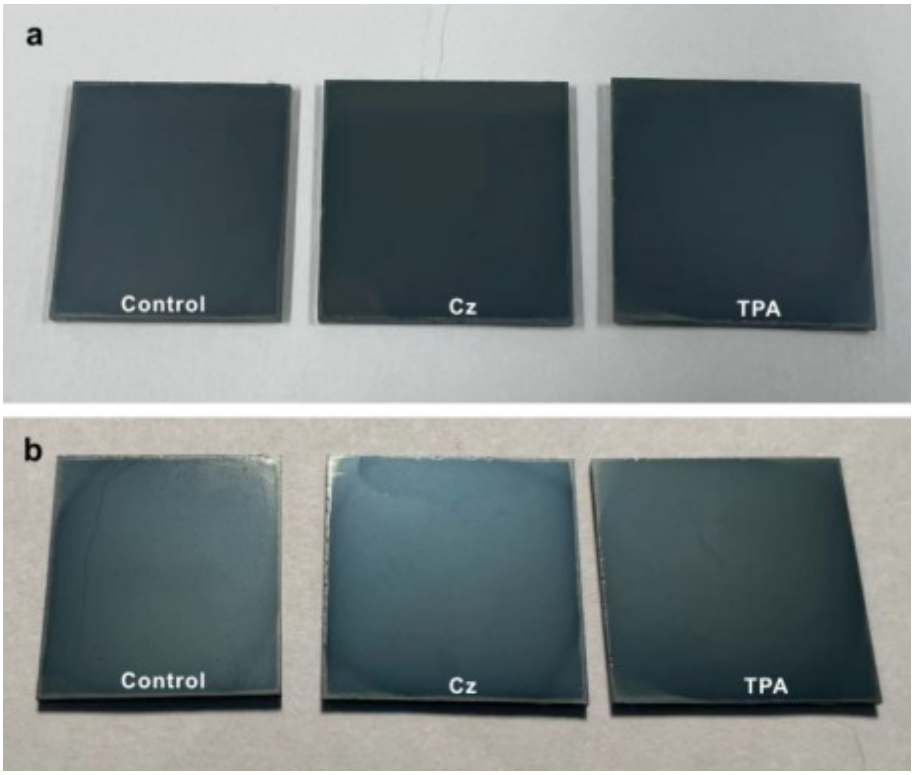


Fig. S25. Images of perovskite films without and with Cz, TPA modification before (a) and after (b) 100 hours of UV light irradiation (~40% humidity).

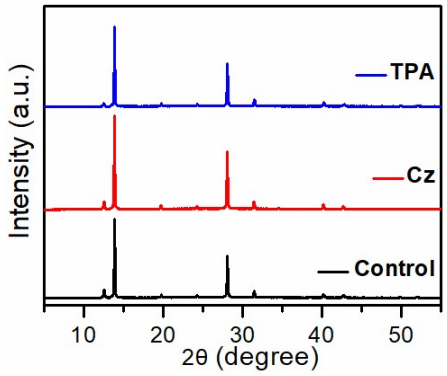


Fig. S26. XRD patterns of the perovskite films without and with Cz, TPA modification after 100 hours of UV light irradiation (~40% humidity). Compared to the control sample and Cz-treated sample, the perovskite film modified by TPA reveals the obviously reduced peaks of $PbI_2$ at 12.6°.

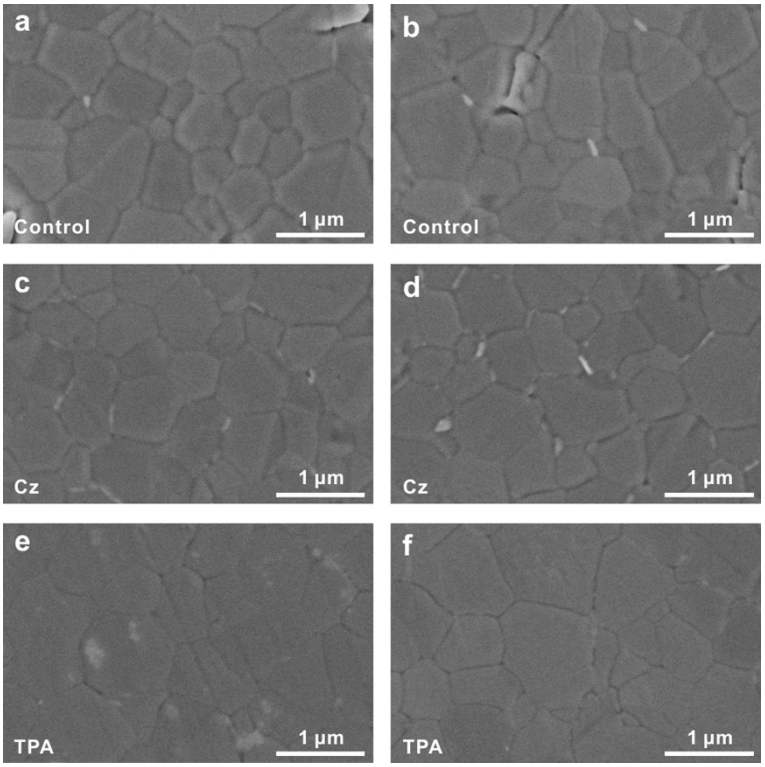


Fig. S27. SEM images of buried interfaces for perovskite films without (a, b) and with Cz (c, d), TPA (e, f) modification before (Left) and after (Right) 100 hours of UV light irradiation (~40% humidity).

## 3. Supporting tables

Table S1. Dipole moment (Debye) decomposition analysis by molecular fragments of TPA and Cz.

| Molecules | left | right | Total | N atoms |
|---|---|---|---|---|
| TPA | 4.5 | 1.66 | 6.13 | 3.360869 |
| Cz | 4.1 | 0.43 | 3.73 | 3.808554 |

Table S2. The cyano group restrained electrostatic potential charge of perovskite with TPA and Cz.

| System | RESP charge | RESP charge |
|---|---|---|
| Cz-perovskite | -0.279803 | -0.531026 |
| TPA-perovskite | -0.279006 | -0.771971 |

Table S3. RMSD with cubic perovskite with TPA and Cz.

| System | RMSD |
|---|---|
| Cz-perovskite | 53.16 $A^2$ |
| TPA-perovskite | 14.15 $A^2$ |

Table S4. Photovoltaic parameters of PSCs based on $SnO_2$ substrates treated with different materials (with an active area of 0.1 $cm^2$).

| Devices | | $J_{sc}$/mA·$cm^{-2}$ | Voc/V | FF/% | PCE/% |
|---|---|---|---|---|---|
| Control | Reverse | 25.29 | 1.174 | 79.43 | 23.58 |
| | Forward | 25.35 | 1.172 | 77.89 | 23.15 |
| Cz | Reverse | 25.49 | 1.185 | 81.62 | 24.65 |
| | Forward | 25.29 | 1.181 | 81.23 | 24.26 |
| TPA | Reverse | 25.30 | 1.203 | 84.35 | 25.67 |
| | Forward | 25.44 | 1.199 | 82.32 | 25.12 |

Table S5. Summary of the photovoltaic parameters for the reported cells and modules.

| | Cell | Module | FF (%) | Perovskite | Ref. |
|---|---|---|---|---|---|
| 1 | 25.6 | 21.55 | 79.70 | $Cs_{0.05}FA_{0.9}MA_{0.05}PbI_3$ | 11 |
| 2 | 25.04 | 21.95 | 80.27 | $FA_{0.9}MA_{0.03}Cs_{0.07}$ $Pb(I_{0.975}Br_{0.025})_3$ | 12 |
| 3 | 25.04 | 21.48 | 80.3 | $Cs_{0.05}MA_{0.05}FA_{0.9}PbI_3$ | 13 |
| 4 | 24.6 | 21.8 | 79.5 | $FA_{0.9}Cs_{0.1}PbI_3$ | 14 |
| 5 | 23.5 | 19.6 | 73.8 | $Cs_{0.05}FA_{0.85}MA_{0.10}Pb(I_{0.97}Br_{0.03})_3$ | 15 |
| 6 | 25 | 21.4 | 74.22 | $Cs_{0.05}MA_{0.05}FA_{0.9}PbI_3$ | 16 |
| 7 | 25.4 | 22 | 76.9 | $Cs_{0.05}(FA_{0.95}MA_{0.05})_{0.95}Pb(I_{0.95}Br_{0.05})_3$ | 17 |
| 8 | 25.2 | 21 | 78.7 | $FAPbI_3$ | 18 |
| 9 | 25.09 | 20.23 | 80.50 | $FAPbI_3$ | 19 |
| 10 | 25.24 | 21.78 | 77.75 | $Cs_{0.05}MA_{0.05}FA_{0.9}PbI_3$ | 20 |
| 11 | 24.9 | 20.91 | 78.31 | $(FAPbI_3)_{0.967}(CsPbI_3)_{0.025}(MAPbBr_3)_{0.008}$ | 21 |
| 12 | 24.9 | 21.2 | 73.5 | $FAPbI_3$ | 22 |
| 13 | 25.2 | 20.66 | 73.80 | $FAPbI_3$ | 23 |
| 14 | 23.21 | 21.37 | 80.89 | $Cs_{0.05}(FA_{0.9}MA_{0.1})_{0.95}Pb(I_{0.9}Br_{0.1})_3$ | 24 |
| 15 | 25.4 | 21.7 | 77.90 | $FAPbI_3$ | 25 |
| **16** | **25.09** | **22.83** | **82.02** | **$Cs_{0.08}FA_{0.92}PbI_3$** | **This work** |

Table S6. Efficiency statistical analyses of 15 modules with TPA.

| Modules | Area ($cm^2$) | | $V_{oc}$ (V) | $I_{sc}$ (mA) | *FF* (%) | PCE (%) |
|---|---|---|---|---|---|---|
| 1 | | Reverse | 6.001 | 54.02 | 79.28 | 22.53 |
| 2 | | Reverse | 6.011 | 54.50 | 79.37 | 22.71 |
| 3 | | Reverse | 6.025 | 55.85 | 79.38 | 23.32 |
| 4 | | Reverse | 6.003 | 53.85 | 80.22 | 22.63 |
| 5 | | Reverse | 6.006 | 53.71 | 80.53 | 22.68 |
| 6 | | Reverse | 5.993 | 53.90 | 80.38 | 22.66 |
| 7 | | Reverse | 6.054 | 51.32 | 83.04 | 22.53 |
| 8 | 11.46 | Reverse | 6.045 | 54.69 | 81.07 | 23.41 |
| 9 | | Reverse | 6.043 | 52.51 | 82.37 | 22.82 |
| 10 | | Reverse | 5.998 | 55.47 | 79.69 | 23.15 |
| 11 | | Reverse | 6.044 | 53.09 | 81.65 | 22.88 |
| 12 | | Reverse | 6.056 | 53.78 | 81.26 | 23.11 |
| 13 | | Reverse | 6.032 | 53.08 | 81.88 | 22.89 |
| 14 | | Reverse | 6.011 | 54.50 | 79.37 | 22.71 |
| 15 | | Reverse | 6.039 | 54.71 | 80.14 | 23.12 |

Table S7. Photovoltaic parameters of solar modules with $Cs_{0.05}MA_{0.05}FA_{0.9}PbI_3$ perovskite system (the areas mentioned below all refer to the aperture area).

| Modules | Area ($cm^2$) | | $V_{oc}$ (V) | $I_{sc}$ (mA) | *FF* (%) | PCE (%) |
|---|---|---|---|---|---|---|
| Control | 11.46 | Reverse | 5.926 | 54.12 | 76.41 | 21.38 |
| | | Forward | 5.910 | 54.25 | 72.37 | 20.26 |
| TPA | 11.46 | Reverse | 6.045 | 54.69 | 81.07 | 23.41 |
| | | Forward | 6.027 | 54.91 | 79.95 | 23.11 |
| TPA | 72.00 | Reverse | 14.37 | 140.94 | 77.94 | 21.91 |
| | | Forward | 14.31 | 143.56 | 75.51 | 21.55 |
| CsFAMA | 12.55 | Reverse | 7.223 | 50.53 | 80.37 | 23.37 |
| | | Forward | 7.204 | 50.68 | 78.06 | 22.71 |

## 4. Supporting references


1. G. Fu, D.-K. Lee, C. Ma and N.-G. Park, *ACS Energy Lett.*, 2023, **8**, 4563-4571.
2. Y. Li, P. Han, X. Zhang, J. Zhou, X. Qiao, D. Yang, A. Qin, B. Z. Tang, J. Peng and D. Ma, *J. Mater. Chem. C*, 2023, **11**, 3284-3291.
3. X. Guo, P. Yuan, J. Fan, X. Qiao, D. Yang, Y. Dai, Q. Sun, A. Qin, B. Z. Tang and D. Ma, *Adv. Mater.*, 2021, **33**, 202006953.
4. W. Kohn and L. J. Sham, *Physical Review*, 1965, **140**, A1133-A1138.
5. J. VandeVondele, M. Krack, F. Mohamed, M. Parrinello, T. Chassaing and J. Hutter, *Computer Physics Communications*, 2005, **167**, 103-128.
6. J. Hutter, M. Iannuzzi, F. Schiffmann and J. VandeVondele, *WIREs Computational Molecular Science*, 2013, **4**, 15-25.
7. S. Goedecker, M. Teter and J. Hutter, *Physical Review B*, 1996, **54**, 0163-1829.
8. T. H. Dunning, *J. Chem. Phys.*, 1989, **90**, 1007-1023.
9. T. Lu and F. Chen, *Journal of Computational Chemistry*, 2011, **33**, 580-592.
10. C. I. Bayly, P. Cieplak, C. Wendy D and P. A. Kollman, *J. Phys. Chem.*, 1993, **97**, 10269-10280.
11. Y. Yang, C. Liu, Y. Ding, B. Ding, J. Xu, A. Liu, J. Yu, L. Grater, H. Zhu, S. S. Hadke, V. K. Sangwan, A. S. R. Bati, X. Hu, J. Li, S. M. Park, M. C. Hersam, B. Chen, M. K. Nazeeruddin, M. G. Kanatzidis and E. H. Sargent, *Nat. Energy*, 2024, **9**, 316-323.
12. D. Liu, C. Chen, X. Wang, X. Sun, B. Zhang, Q. Zhao, Z. Li, Z. Shao, X. Wang, G. Cui and S. Pang, *Adv. Mater.*, 2023, DOI: 10.1002/adma.202310962, 202310962.
13. W. Yang, B. Ding, Z. Lin, J. Sun, Y. Meng, Y. Ding, J. Sheng, Z. Yang, J. Ye, P. J. Dyson and M. K. Nazeeruddin, *Adv. Mater.*, 2023, **35**, 202302071.
14. C. Fei, N. Li, M. Wang, X. Wang, H. Gu, B. Chen, Z. Zhang, Z. Ni, H. Jiao, W. Xu, Z. Shi, Y. Yan and J. Huang, *Science*, 2023, **380**, 823-829.
15. S. You, H. Zeng, Y. Liu, B. Han, M. Li, L. Li, X. Zheng, R. Guo, L. Luo, Z. Li, C. Zhang, R. Liu, Y. Zhao, S. Zhang, Q. Peng, T. Wang, Q. Chen, F. T. Eickemeyer, B. Carlsen, S. M. Zakeeruddin, L. Mai, Y. Rong, M. Grätzel and X. Li, *Science*, 2023, **379**, 288-294.
16. P. Shi, Y. Ding, B. Ding, Q. Xing, T. Kodalle, C. M. Sutter-Fella, I. Yavuz, C. Yao, W. Fan, J. Xu, Y. Tian, D. Gu, K. Zhao, S. Tan, X. Zhang, L. Yao, P. J. Dyson, J. L. Slack, D. Yang, J. Xue, M. K. Nazeeruddin, Y. Yang and R. Wang, *Nature*, 2023, **620**, 323-327.
17. S. Zhang, F. Ye, X. Wang, R. Chen, H. Zhang, L. Zhan, X. Jiang, Y. Li, X. Ji, S. Liu, M. Yu, F. Yu, Y. Zhang, R. Wu, Z. Liu, Z. Ning, D. Neher, L. Han, Y. Lin, H. Tian, W. Chen, M. Stolterfoht, L. Zhang, W.-H. Zhu and Y. Wu, *Science*, 2023, **380**, 404-409.
18. S. Yu, Z. Xiong, H. Zhou, Q. Zhang, Z. Wang, F. Ma, Z. Qu, Y. Zhao, X. Chu, X. Zhang and J. You, *Science*, 2023, **382**, 1399-1404.
19. Y. Miao, M. Ren, Y. Chen, H. Wang, H. Chen, X. Liu, T. Wang and Y. Zhao,

*Nat. Sustain.*, 2023, **6**, 1465-1473.

20. X. Liu, B. Ding, M. Han, Z. Yang, J. Chen, P. Shi, X. Xue, R. Ghadari, X. Zhang, R. Wang, K. Brooks, L. Tao, S. Kinge, S. Dai, J. Sheng, P. J. Dyson, M. K. Nazeeruddin and Y. Ding, *Angew. Chem. Int. Ed.*, 2023, **62**, e202304350.
21. H. Xu, Z. Liang, J. Ye, Y. Zhang, Z. Wang, H. Zhang, C. Wan, G. Xu, J. Zeng, B. Xu, Z. Xiao, T. Kirchartz and X. Pan, *Energy Environ. Sci.*, 2023, **16**, 5792-5804.
22. F. Ye, T. Tian, J. Su, R. Jiang, J. Li, C. Jin, J. Tong, S. Bai, F. Huang, P. Müller-Buschbaum, Y. B. Cheng and T. Bu, *Adv. Energy Mater.*, 2023, **14**, 202302775.
23. K. Zhang, Y. Wang, M. Tao, L. Guo, Y. Yang, J. Shao, Y. Zhang, F. Wang and Y. Song, *Adv. Mater.*, 2023, **35**, 202211593.
24. Y. Gao, C. Liu, M. He, C. Zhang, L. Liu, Q. Luo, Y. Wu, H. Zhang, X. Zhong, R. Guo, Y. Xie, S. Wu, R. E. I. Schropp and Y. Mai, *Adv. Mater.*, 2023, **36**, 2309310.
25. M. Kim, J. Jeong, H. Lu, T. K. Lee, F. T. Eickemeyer, Y. Liu, I. W. Choi, S. J. Choi, Y. Jo, H.-B. Kim, S.-I. Mo, Y.-K. Kim, H. Lee, N. G. An, S. Cho, W. R. Tress, S. M. Zakeeruddin, A. Hagfeldt, J. Y. Kim, M. Grätzel and D. S. Kim, *Science*, 2022, **375**, 302-306.